

SpACNN-LDVAE: Spatial Attention Convolutional Latent Dirichlet Variational Autoencoder for Hyperspectral Pixel Unmixing

Soham Chitnis^{1,2*}, Kiran Mantripragada², and Faisal Z. Qureshi²

¹ Department of Computer Science & Information Systems, Birla Institute of Technology and Science, Pilani, India
f20201723@goa.bits-pilani.ac.in

² Faculty of Science, Ontario Tech University, Oshawa, Canada
{kiran.mantripragada,faisal.qureshi}@ontariotechu.ca

Abstract. The Hyperspectral Unmixing problem is to find the pure spectral signal of the underlying materials (endmembers) and their proportions (abundances). The proposed method builds upon the recently proposed method, Latent Dirichlet Variational Autoencoder (LDVAE). It assumes that abundances can be encoded as Dirichlet Distributions while mixed pixels and endmembers are represented by Multivariate Normal Distributions. However, LDVAE does not leverage spatial information present in an HSI; we propose an Isotropic CNN encoder with spatial attention to solve the hyperspectral unmixing problem. We evaluated our model on Samson, Hydice Urban, Cuprite, and OnTech-HSI-Syn-21 datasets. Our model also leverages the transfer learning paradigm for Cuprite Dataset, where we train the model on synthetic data and evaluate it on real-world data. We are able to observe the improvement in the results for the endmember extraction and abundance estimation by incorporating the spatial information. Code can be found at <https://github.com/faisalqureshi/cnn-ldvae>

Keywords: Hyperspectral image analysis · Unmixing · Endmember Extraction · Abundance Estimation · Variational Autoencoder · Deep Learning · Isotropic CNN Encoder · Spatial Attention Convolution

1 Introduction

Hyperspectral Images can be applied in a variety of applications and are very prominent in the field of remote sensing. They are known for having lower spatial resolution but very high spectral resolution. The lower spatial resolution implies that a single pixel covers a large region of space [1]. Such a phenomenon is mostly attributed to the images collected from high altitudes. The pixel unmixing task is to infer the materials with their mixing ratios. This problem is of particular interest to the hyperspectral image analysis community. In literature, it is sometimes referred to as *spectral unmixing* [2]. It involves recovering

* Supported by MITACS Globalink Research Internship

the "pure" spectra of materials known as endmembers with the ratios of mixing known as abundances.

Existing methods can be divided into (1) Data-driven Methods and (2) Physics-based Methods. Data-driven methods attempt to decompose a pixel into spectra of various end members. Some examples of such techniques are Blind Source Separation (BSS), analysis of principal components linear or non-linear, and Linear Discriminant analysis [3]–[6]. Physics-based Methods use phenomenological models for the radiance response of the materials [1], [7]. It is tedious to construct physics-based models that would work accurately for different materials.

Many well-established approaches such as N-FINDR [8], PPI (Pixel Purity Index) [9], and Vector Component Analysis [10] follow a two-step process: extract the endmembers first, followed by abundance estimation. These aforementioned methods first extract the endmembers that must followed by a least squares method to compute the abundances, being the Fully Constrained Least Squares [11] the most common approach as it applies both necessary constraints for the n-simplex form of abundances vectors: Abundances-sum-to-one constraint (ASC), and Abundances-non-negative constraint (ANC).

From training aspects, a number of existing methods are unsupervised, such as Blind Source Separation (BSS), but still alone cannot identify materials; therefore, they require a search within a database to identify the specific underlying categorical target. On the other hand, our method can identify endmember classes, but it is supervised and requires labels for model training.

Most existing methods do not use deep learning, such as Linear Mixing models (LMM), Perturbed LMM (PLMM), Extended LMM (ELMM), Nonlinear LMM (NLMM), and data-driven LMM [12]–[16]. With the rapid development in machine learning and deep learning, newer Deep Learning methods have been proposed for the unmixing problem, such as EACNN [17], DAEN [18], and TANet [19]. We propose a data-driven deep learning-based approach for the unmixing problem.

This paper builds on the work of the Latent Dirichlet Variation Autoencoder (LDVAE) [20], which assumes the endmember spectra can be represented using multivariate Normal Distribution and the mixing ratios (abundances) can be represented using Dirichlet Distribution. While LDVAE is a simple MLP model that does not incorporate spatial information, our approach explores spatial information, as it is usually observed that nearby pixels may have similar mixing ratios. For this task, we incorporate spatial information of each pixel using an Isotropic CNN encoder with Spatial Attention in the encoder stage that can be trained to represent the pixels in a reduced-size latent vector while also representing the abundance ratios. We will be referring to the simple LDVAE model as MLP-LDVAE.

2 Related Works

Previous works can be classified into physical and data-driven models. Some recent methods presenting state-of-the-art results are also based on the Non-Negative Matrix Factorization method (NMF), which tries to determine endmembers and abundances in a single optimization framework. The key idea is to break a non-negative matrix into two non-negative matrices. Some works are improving NMF methods with regularization.

Spectral-Spatial Weighted Sparse Non-Negative Matrix Factorization (SS-WNMF) [3] uses spatial information when performing pixel unmixing with the usual NMF method. For any given pixel, the spatial information is collected from the neighboring pixels using a weighted window strategy.

Spatial Group Sparsity Regularized Non-negative Matrix Factorization (SGSNMF) [21] uses the contextual cues from clusters of hyperspectral pixels. Within a proximate spatial cluster, it is found that pixels exhibit analogous patterns in the matrix (abundance). The arrangement of such clusters is established through image segmentation. As opposed to using predetermined shapes for grouping, like crosses or squares, the spatial clusters are dynamically defined by means of superpixels.

The Total Variation Regularized Re-weighted Sparse Nonnegative Matrix Factorization (TV-RSNMF) [22] investigates the sparsity characteristics of abundance maps within NMF using a weighted sparse model.

Graph Regularized $L_{1/2}$ -NMF (GLNMF) [23] is a two-step approach with sparse constraint and a graph regularization. $L_{1/2}$ regularizer enforces the sparsity of material abundances; this is the first step. The second step builds a nearest-neighbor graph to model the local structural information for hyperspectral unmixing.

With the recent progress in Deep Learning, more recent deep learning-based methods are available for hyperspectral unmixing. Most of these methods are Autoencoder based and only focus on solving the hyperspectral unmixing problem and use VCA as a preliminary step for processing information.

EACNN [17] is a deep-learning-based approach that has achieved state-of-the-art results. EACNN has two networks: the Endmember network and the Unmixing network. For the endmember extraction problem, they first use Vector Component Analysis to cluster the endmembers into endmember bundles, which are used to train the endmember network. The unmixing network has two components: the unmixing module and the reconstruction module. The last layer of the endmember network is shared with the last layer of the unmixing module. This follows a two-step process similar to VCA with FCLS.

DeepGUn [24] is a deep learning method for pixel unmixing. For endmember extraction, vector component analysis is used. The paper investigates using regularization methods for the same. Using these endmembers deep learning models are trained enabling the reconstruction of pure signal. This is similar to EACNN.

We do not employ any separate method for endmember extraction. To the best of our knowledge, recent works do not focus on generating hyperspectral data. Obtaining labeled hyperspectral data for unmixing is extremely tedious,

so we propose a Variational Autoencoder that could be used for the unmixing problem and generating new synthetic data in the future.

3 Methodology

Latent Dirichlet Variational Autoencoder is inspired by Latent Dirichlet Allocation (LDA) [25]. In LDA, we have a document that can be composed of a set of topics, but we do not know the mixing proportions of these topics that generated the document. This is analogous to pixel unmixing, where these topics are the endmembers and documents are the pixels themselves. The aim of LDA is to discover the latent topics and estimate to what degree each topic contributes. The first task is similar to the endmember extraction, and the second is to the abundance estimation.

3.1 CNN Latent Dirichlet Variational Autoencoder

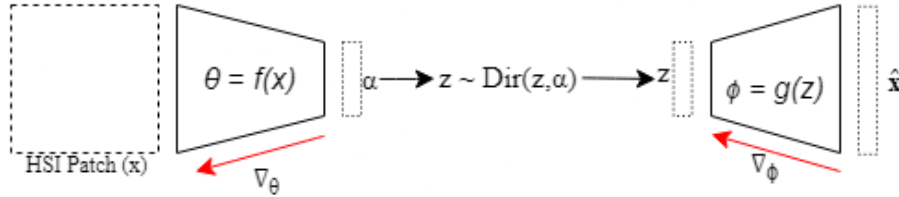


Fig. 1. CNN Latent Dirichlet Variational Autoencoder

Our model uses the VAE Architecture as Figure 1. LDVAE is a Variational Autoencoder where the latent representation follows a Dirichlet distribution. The encoder is parameterized by θ , which outputs the Dirichlet distribution parameter α . LDVAE takes a single signal of the pixel. We now try to leverage spatial information in the encoder using a CNN.

3.2 Spatial Attention Convolutional Neural Network Encoder

Our model uses the CNN encoder as Figure 2. It inputs a patch of HSI data and outputs the Dirichlet Distribution parameter α corresponding to the middle pixel of the patch. The abundances \mathbf{z} are sampled from the Dirichlet distribution and fed into the decoder, which reconstructs the spectral signal of the middle pixel $\hat{\mathbf{x}}$.

CNN model is an isotropic model, i.e., it always maintains the spatial resolution. The CNN encoder has 3 major sections: (1) Stem, (2) Body (3) Spatial

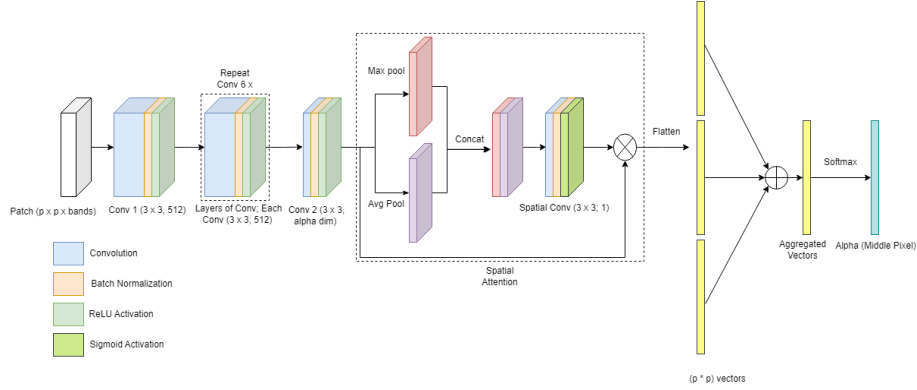


Fig. 2. Spatial Attention Convolutional Neural Network Encoder

Attention branch. In the Stem section, there is a 2D Convolution Layer with a kernel of size 3 and padding 1 with Batch Normalization and ReLU activation. The Body comprises 6 blocks of Convolution layer, Batch Normalization, and activation ReLU. CBAM introduced Spatial Attention [26]. We use spatial attention in our Spatial Attention block. Finally, we aggregate the vectors and generate the Dirichlet parameter α . The mathematical equations which define Spatial Attention as follows:

Given the intermediate feature map $F \in \mathbb{R}^{H \times W \times C}$, first average and max pooling is applied along the channel dimension, then concatenate them along the channel dimension. Followed by a 2D Convolution operation with a kernel size of 3 and sigmoid activation to obtain a 2D Spatial Attention Map.

$$\begin{aligned} A &= \sigma(f^{3 \times 3}([AvgPool(M_{Sa}(F)); MaxPool(M_{Sa}(F))])) \\ &= \sigma(f^{3 \times 3}([F_{Avg}^{Sa}; F_{Max}^{Sa}])) \end{aligned} \quad (1)$$

where σ denotes the sigmoid function and $f^{3 \times 3}$ denotes the convolution operation with a filter of 3×3 .

The computed vectors are aggregated using the attention map as follows:

$$z' = \sum_{i=1}^k \sum_{j=1}^k a_{i,j} F_{i,j} \quad (2)$$

where k is the size of the patch and $a_{i,j}$ is the attention weight, $F_{i,j}$ is vector at i, j location.

To ensure the model satisfies the Abundance Sum Constraint (ASC) and Abundance Non-Negative Constraint (ANC), i.e., the ratio should add up to 1, and it should be non-negative, a final Softmax Activation is applied to obtain alpha.

$$\alpha_i = \frac{e^{z'_i}}{\sum_{i=1}^C e^{z'_i}} \quad (3)$$

3.3 Spectral Reconstruction With Multivariate Normal Distribution

The decoder is the same as LDVAE. It reconstructs the spectra given the \mathbf{z} , i.e., abundances. The decoder serves two purposes: (1) to construct spectra given previously unseen combinations of abundances, and (2) the decoder can solve the endmember extraction problem. The model assumes that spectra follow a multivariate Normal Distribution as below:

$$\begin{aligned} \mathbf{x} &\sim Normal(\mathbf{x}; \boldsymbol{\mu}, \boldsymbol{\Sigma}) \text{ where} \\ \mathbf{x} &= \{x_1, x_2, x_3, \dots, x_k\} \\ \boldsymbol{\mu} &= \{\mu_1, \mu_2, \mu_3, \dots, \mu_k\} \\ \boldsymbol{\Sigma} &= \text{diag}(\sigma_1, \sigma_2, \sigma_3, \dots, \sigma_k) \end{aligned} \quad (4)$$

3.4 Loss function

Normally, VAEs are trained in an unsupervised setting, but the model is trained with supervision for the abundance estimation. Since the model reconstructs the spectra signal and the model is a VAE, the loss has 2 components: (1) Reconstruction loss for abundances and (2) ELBO Loss for the VAE. The reconstruction loss for abundance is a Mean Squared Error (MSE) and is represented as follows:

$$\mathcal{L}(\hat{\mathbf{z}}, \mathbf{z}) = (\mathbf{z} - \hat{\mathbf{z}})^2 \quad (5)$$

and ELBO Loss is represented as follows:

$$\mathcal{L}(\mathbf{x}; \theta, \phi) = \mathbb{E}_{q_\theta} [\log p_\phi - KL(q_\theta(z|x)||p(z))] \quad (6)$$

The first term on the right side is the reconstruction loss for the signal, and the KL divergence term is to minimize the distance between the distribution induced by latent representation and the desired distribution. For more details on KL Divergence with Dirichlet distribution, refer to [20], and for ELBO loss derivation, refer to [27]–[30].

4 Empirical Evaluation

4.1 Datasets

Samson Samson is 95×95 , 156-channel hyperspectral image [31]. This dataset contains three endmembers: soil, tree, and water. The training and testing set is 80:20 split.

Urban (HYDICE) Urban (HYDICE) dataset is a well-known dataset for hyperspectral unmixing [32]. It is 307×307 , 162-channel hyperspectral image covering a 2×2 m². This dataset has three versions, containing four, five, and six endmembers. In this work six endmember is used. The training and testing split used is 80:20.

Cuprite The Cuprite dataset [33] covers the region around Las Vegas, Nevada, US. It is a 512×614 , 188-channel hyperspectral image. The dataset contains twelve minerals (endmembers): *Alunite*, *Andradite*, *Buddingtonite*, *Dumortierite*, *Kaolinite1*, *Kaolinite2*, *Muscovite*, *Montmorillonite*, *Nontronite*, *Pyrope*, *Sphene*, and *Chalcedony*. This dataset does not have ground truth abundances. Therefore, for training, we use a Synthetically generated dataset. For more details on synthetic dataset, refer to [20]. The model is trained on Synthetic data and tested on the Cuprite dataset.

OnTech-HSI-Syn-21 This is a synthetic dataset containing the following nine endmembers: *Adularia GDS57*, *Jarosite GDS99*, *Jarosite GDS101*, *Anorthite HS349.1B*, *Calcite WS272*, *Alunite GDS83*, *Howlite GDS155*, *Corrensite CorWa-1*, and *Fassaite HS118.3B*. It is 128×128 , 224-channel hyperspectral image. For more details, refer to [20].

4.2 Metrics

Spectral Angle Distance (SAD) The SAD metric is a distance measurement between two spectral signals and is given as follows:

$$SAD = \arccos\left(\frac{\hat{\mathbf{x}}_e^T \mathbf{x}_e}{\|\hat{\mathbf{x}}_e\| \|\mathbf{x}_e\|}\right) \quad (7)$$

where $\hat{\mathbf{x}}_e$ represents the endmember (spectral signal) generated and \mathbf{x}_e is the ground truth endmember. This metric computes the accuracy of endmember extraction. In our experiments, we use SAD to evaluate the quality of the endmembers extracted for each material in the dataset.

Root Mean Square Error (RMSE) RMSE is used to evaluate abundance estimation accuracy. It is computed as follows:

$$RMSE = \sqrt{\frac{1}{N} \sum_{n=1}^N (\mathbf{z}_n - \hat{\mathbf{z}}_n)^2} \quad (8)$$

Here, \mathbf{z} is the ground truth abundances, and $\hat{\mathbf{z}}$ is generated abundances. N denotes the number of pixels used in the computation.

4.3 Algorithms and Machines

All models were trained using an NVIDIA V100-SXM2 Machine. For the implementation of LDVAE, we use Pyro python library, a probabilistic programming framework based on PyTorch [34].

5 Results

The results on all four datasets are reported. We report the RMSE and SAD metrics for the individual elements and the overall average metric. Table 1 contains the results on Samson Dataset. Table 2 reports results on the HYDICE Urban Dataset. Both RMSE and SAD metrics have improved from MLP-LDVAE for the Samson and HYDICE Urban Dataset. As Cuprite does not have abundances, we do not report the same. Its SAD metric is reported in Table 3. The results for the endmember extraction problem are significantly improved with LDVAE for the Cuprite Dataset. The results of the OnTech-Syn-HSI-21 Dataset are reported in Table 4. Both RMSE and SAD metrics have improved from MLP-LDVAE for the OnTech-Syn-HSI-21 Dataset. Across all datasets, our method has a lower standard deviation than previous works.

Table 1. Results on Samson Dataset

		SpACNN-LDVAE	MLP-LDVAE	VCA+FCLS	PLMM	ELMM	GLMM	DeepGUN	EACNN
Soil	RMSE	0.2522 ± 0.00	0.2609 ± 0.00	-	-	-	-	-	-
	SAD	0.2097 ± 0.01	0.0959 ± 0.10	-	-	-	-	-	0.0328
Tree	RMSE	0.2614 ± 0.00	0.3431 ± 0.00	-	-	-	-	-	-
	SAD	0.5347 ± 0.03	1.2788 ± 1.28	-	-	-	-	-	0.0519
Water	RMSE	0.2098 ± 0.00	0.3165 ± 0.00	-	-	-	-	-	-
	SAD	0.8233 ± 0.04	0.4022 ± 0.40	-	-	-	-	-	0.1026
Average	RMSE	0.2412 ± 0.00	0.3078 ± 0.00	0.0545	0.0239	0.0119	0.0006	0.0862	0.0171
	SAD	0.5525 ± 0.03	0.5923 ± 0.59	-	-	-	-	-	0.0624

Table 2. Results on HYDICE Urban Dataset

		SpACNN-LDVAE	MLP-LDVAE	SSWNMF	SGSNMF	TV-RSNMF	RSNMF	GLNMF	L1/2-NMF	VCA+FCLS
Asphalt	RMSE	0.1566 ± 0.00	0.2889 ± 0.00	-	-	-	-	-	-	-
	SAD	0.2786 ± 0.02	0.4263 ± 0.43	0.0782 ± 3.29	0.0841 ± 4.01	0.0770 ± 2.97	0.0869 ± 3.81	0.1008 ± 3.19	0.0889 ± 2.88	0.2246 ± 3.44
Road	RMSE	0.1977 ± 0.00	0.1832 ± 0.00	-	-	-	-	-	-	-
	SAD	0.1936 ± 0.01	0.3323 ± 0.33	0.1490 ± 3.58	0.1516 ± 3.25	0.1495 ± 3.54	0.1594 ± 3.62	0.1531 ± 3.06	0.1452 ± 3.57	0.1981 ± 3.39
Grass	RMSE	0.1632 ± 0.00	0.1737 ± 0.00	-	-	-	-	-	-	-
	SAD	0.4411 ± 0.04	0.3177 ± 0.32	0.1173 ± 3.46	0.1199 ± 3.36	0.1269 ± 4.02	0.1457 ± 4.29	0.1424 ± 3.79	0.1509 ± 3.18	0.2137 ± 2.41
Tree	RMSE	0.1283 ± 0.00	0.1250 ± 0.00	-	-	-	-	-	-	-
	SAD	0.4502 ± 0.03	0.4393 ± 0.44	0.0713 ± 3.61	0.0731 ± 3.54	0.0746 ± 4.09	0.0849 ± 3.90	0.0986 ± 4.62	0.0863 ± 4.06	0.2673 ± 3.77
Roof	RMSE	0.0992 ± 0.00	0.2599 ± 0.00	-	-	-	-	-	-	-
	SAD	0.3242 ± 0.02	0.7004 ± 0.70	0.1241 ± 2.76	0.1250 ± 3.81	0.1247 ± 3.53	0.1324 ± 4.15	0.1370 ± 4.28	0.1334 ± 3.90	0.1848 ± 3.68
Metal	RMSE	0.1842 ± 0.00	0.1334 ± 0.00	-	-	-	-	-	-	-
	SAD	0.2026 ± 0.01	0.2806 ± 0.28	0.0802 ± 3.17	0.0859 ± 3.91	0.0849 ± 3.92	0.0798 ± 3.77	0.1059 ± 3.96	0.1063 ± 3.54	0.1992 ± 3.43
Dirt	RMSE	0.1558 ± 0.00	0.1840 ± 0.00	0.0048 ± 0.72	0.0061 ± 0.67	0.0055 ± 0.81	0.0053 ± 0.98	0.0069 ± 0.85	0.0044 ± 0.76	0.0119 ± 0.66
	SAD	0.3151 ± 0.02	0.4161 ± 0.42	0.1034 ± 3.31	0.1060 ± 3.68	0.1063 ± 3.68	0.1148 ± 3.92	0.1230 ± 3.52	0.1185 ± 3.52	0.2142 ± 3.35

Table 3. Results on Cuprite Dataset

		SpACNN-LDVAE	MLP-LDVAE	SSWNMF	SGSNMF	TV-RSNMF	RSNMF	GLNMF	L1/2-NMF	VCA+FCLS
alunite		0.0683 ± 0.00	0.0097 ± 0.01	0.1497 ± 3.97	0.1238 ± 4.01	0.1204 ± 4.37	0.1189 ± 4.39	0.1353 ± 3.83	0.1496 ± 3.32	0.1574 ± 3.71
Andradite		0.0462 ± 0.00	0.0381 ± 0.04	-	-	-	-	-	-	-
Buddingtonite		0.0227 ± 0.00	0.0051 ± 0.01	0.0958 ± 4.69	0.1021 ± 3.47	0.0903 ± 5.08	0.1342 ± 4.72	0.1437 ± 3.62	0.1441 ± 4.16	0.1412 ± 3.74
Dumortierite		0.0500 ± 0.00	0.1922 ± 0.19	-	-	-	-	-	-	-
Kaolinite_1		0.0740 ± 0.00	0.0258 ± 0.03	0.0885 ± 2.94	0.0986 ± 3.18	0.1097 ± 3.47	0.0955 ± 3.07	0.0967 ± 4.01	0.0825 ± 4.66	0.0736 ± 4.42
Kaolinite_2		0.0249 ± 0.00	0.0699 ± 0.07	0.1206 ± 3.67	0.1375 ± 3.48	0.1213 ± 3.82	0.1396 ± 4.11	0.1356 ± 3.91	0.1402 ± 4.18	0.1420 ± 4.16
Muscovite		0.0320 ± 0.00	0.0064 ± 0.01	0.1024 ± 4.24	0.1061 ± 3.18	0.1131 ± 2.88	0.0997 ± 3.46	0.0961 ± 3.77	0.0889 ± 3.03	0.1007 ± 3.31
Montmorillonite		0.0214 ± 0.00	0.0496 ± 0.05	0.0651 ± 3.08	0.0705 ± 3.36	0.0783 ± 3.95	0.0744 ± 3.12	0.0838 ± 4.28	0.0876 ± 2.91	0.0974 ± 3.39
Nonttronite		0.0639 ± 0.00	0.1048 ± 0.10	0.1138 ± 4.15	0.1046 ± 3.80	0.0911 ± 3.49	0.0832 ± 4.18	0.0953 ± 3.41	0.1038 ± 4.46	0.0772 ± 2.10
Pyrope		0.0342 ± 0.00	0.0156 ± 0.02	0.1106 ± 3.32	0.1208 ± 3.83	0.1253 ± 3.10	0.1469 ± 3.12	0.1318 ± 3.18	0.1123 ± 4.91	0.1437 ± 3.76
Sphene		0.1030 ± 0.00	0.0347 ± 0.03	0.1024 ± 3.79	0.1179 ± 4.02	0.1190 ± 2.97	0.1134 ± 2.54	0.1291 ± 4.21	0.1252 ± 5.18	0.1277 ± 4.08
Chalcedony		0.0281 ± 0.00	0.055 ± 0.01	0.1496 ± 4.12	0.1221 ± 4.02	0.1387 ± 4.01	0.1224 ± 4.19	0.1341 ± 2.98	0.1520 ± 3.43	0.1514 ± 3.83
Average		0.0470 ± 0.00	0.0465 ± 0.05	0.1099 ± 3.80	0.1104 ± 3.63	0.1107 ± 3.71	0.1128 ± 3.69	0.1182 ± 3.72	0.1186 ± 4.02	0.1212 ± 3.65

Table 4. Results on OnTech-Syn-HSI-21 Dataset

		SpACNN-LDVAE	MLP-LDVAE
adularia-gds57	RMSE	0.1008 ± 0.00	0.0636 ± 0.00
	SAD	0.0276 ± 0.00	0.0984 ± 0.10
jarosite-gds99	RMSE	0.0824 ± 0.00	0.0366 ± 0.00
	SAD	0.0384 ± 0.00	0.0331 ± 0.03
jarosite-gds101	RMSE	0.1043 ± 0.00	0.0522 ± 0.00
	SAD	0.0796 ± 0.00	0.0396 ± 0.04
anorthite-hs349.1b	RMSE	0.1049 ± 0.00	0.0736 ± 0.00
	SAD	0.0277 ± 0.00	0.0148 ± 0.01
calcite-ws272	RMSE	0.0905 ± 0.00	0.0337 ± 0.00
	SAD	0.0359 ± 0.00	0.0142 ± 0.01
alunite-gds83	RMSE	0.0869 ± 0.00	0.0539 ± 0.00
	SAD	0.0528 ± 0.00	0.027 ± 0.03
howlite-gds155	RMSE	0.1158 ± 0.00	0.0463 ± 0.00
	SAD	0.0761 ± 0.00	0.0066 ± 0.01
corrensite-corwa-1	RMSE	0.0859 ± 0.00	0.0547 ± 0.00
	SAD	0.0998 ± 0.00	0.0582 ± 0.06
fassaite-hs118.3b	RMSE	0.0816 ± 0.00	0.0545 ± 0.00
	SAD	0.0972 ± 0.00	0.8797 ± 0.88
Average	RMSE	0.0948 ± 0.00	0.0521 ± 0.00
	SAD	0.0594 ± 0.00	0.1302 ± 0.13

6 Conclusion

This work introduces a spatial attention convolutional LDVAE, which contrasts the previously proposed MLP-LDVAE. Distinctly, it can be noted that most of the previous work’s deep learning methods focused on autoencoder architecture and employed an additional method for the endmember extraction task. We can observe that incorporating spatial information using SpACNN-LDVAE has improved the endmember extraction and abundance estimation problem. As the model is a Variational Autoencoder in future works, it can be extended to generate hyperspectral data using the decoder of LDVAE, given the abundances.

References

- [1] R. Heylen, M. Parente, and P. Gader, “A review of nonlinear hyperspectral unmixing methods,” *Selected Topics in Applied Earth Observations and Remote Sensing, IEEE Journal of*, vol. 7, pp. 1844–1868, Jun. 2014. DOI: 10.1109/JSTARS.2014.2320576.
- [2] E. Maggiori, A. Plaza, and Y. Tarabalka, “Models for hyperspectral image analysis: From unmixing to object-based classification,” in Jan. 2018, pp. 37–80, ISBN: 978-3-319-66328-9. DOI: 10.1007/978-3-319-66330-2_2.
- [3] S. Zhang, G. Zhang, F. Li, *et al.*, “Spectral-spatial hyperspectral unmixing using nonnegative matrix factorization,” *IEEE Transactions on Geoscience and Remote Sensing*, vol. 60, pp. 1–13, 2022. DOI: 10.1109/TGRS.2021.3074364.
- [4] F. Khajehrayeni and H. Ghassemian, “A linear hyperspectral unmixing method by means of autoencoder networks,” *International Journal of Remote Sensing*, vol. 42, pp. 2517–2531, Apr. 2021. DOI: 10.1080/01431161.2020.1854893.
- [5] M. Zhao, X. Wang, J. Chen, and W. Chen, *A plug-and-play priors framework for hyperspectral unmixing*, Dec. 2020.
- [6] A. Plaza and C.-I. Chang, “Fast implementation of pixel purity index algorithm,” *Proceedings of SPIE - The International Society for Optical Engineering*, Jun. 2005. DOI: 10.1117/12.602374.
- [7] J. Plaza, E. Hendrix, I. García Fernández, G. Martín, and A. Plaza, “On endmember identification in hyperspectral images without pure pixels: A comparison of algorithms,” *Journal of Mathematical Imaging and Vision*, vol. 42, pp. 163–175, Feb. 2012. DOI: 10.1007/s10851-011-0276-0.
- [8] M. E. Winter, “N-FINDR: an algorithm for fast autonomous spectral endmember determination in hyperspectral data,” in *Imaging Spectrometry V*, M. R. Descour and S. S. Shen, Eds., ser. Society of Photo-Optical Instrumentation Engineers (SPIE) Conference Series, vol. 3753, Oct. 1999, pp. 266–275. DOI: 10.1117/12.366289.
- [9] J. W. Boardman, F. A. Kruse, and R. O. Green, “Mapping target signatures via partial unmixing of aviris data: In summaries,” 1995. [Online]. Available: <https://api.semanticscholar.org/CorpusID:127556070>.
- [10] J. Nascimento and J. Dias, “Vertex component analysis: A fast algorithm to unmix hyperspectral data,” *IEEE Transactions on Geoscience and Remote Sensing*, vol. 43, no. 4, pp. 898–910, 2005. DOI: 10.1109/TGRS.2005.844293.
- [11] D. C. Heinz and C.-I. Chang, “Fully constrained least squares linear spectral mixture analysis method for material quantification in hyperspectral imagery,” *IEEE Trans. Geosci. Remote. Sens.*, vol. 39, pp. 529–545, 2001. [Online]. Available: <https://api.semanticscholar.org/CorpusID:17214473>.
- [12] M. Veganzones, L. Drumetz, G. Tochon, *et al.*, “A new extended linear mixing model to address spectral variability,” in *2014 6th Workshop on*

- Hyperspectral Image and Signal Processing: Evolution in Remote Sensing (WHISPERS)*, 2014, pp. 1–4. DOI: 10.1109/WHISPERS.2014.8077595.
- [13] L. Drumetz, M.-A. Veganzones, S. Henrot, R. Phlypo, J. Chanussot, and C. Jutten, “Blind hyperspectral unmixing using an extended linear mixing model to address spectral variability,” *IEEE Transactions on Image Processing*, vol. 25, no. 8, pp. 3890–3905, 2016. DOI: 10.1109/TIP.2016.2579259.
- [14] P.-A. Thouvenin, N. Dobigeon, and J.-Y. Tournet, “Hyperspectral unmixing with spectral variability using a perturbed linear mixing model,” *IEEE Transactions on Signal Processing*, vol. 64, no. 2, pp. 525–538, 2016. DOI: 10.1109/TSP.2015.2486746.
- [15] N. Dobigeon, J.-Y. Tournet, C. Richard, J. C. M. Bermudez, S. McLaughlin, and A. O. Hero, “Nonlinear unmixing of hyperspectral images: Models and algorithms,” *IEEE Signal Processing Magazine*, vol. 31, no. 1, pp. 82–94, Jan. 2014. DOI: 10.1109/msp.2013.2279274. [Online]. Available: <https://doi.org/10.1109/msp.2013.2279274>.
- [16] J. S. Bhatt, M. V. Joshi, and M. S. Raval, “A data-driven stochastic approach for unmixing hyperspectral imagery,” *IEEE Journal of Selected Topics in Applied Earth Observations and Remote Sensing*, vol. 7, no. 6, pp. 1936–1946, 2014. DOI: 10.1109/JSTARS.2014.2328597.
- [17] B. Jin, Y. Zhu, W. Huang, Q. Chen, and S. Li, “An efficient attention-based convolutional neural network that reduces the effects of spectral variability for hyperspectral unmixing,” *Applied Sciences*, vol. 12, no. 23, 2022, ISSN: 2076-3417. DOI: 10.3390/app122312158. [Online]. Available: <https://www.mdpi.com/2076-3417/12/23/12158>.
- [18] Y. Su, J. Li, A. Plaza, A. Marinoni, P. Gamba, and S. Chakravorty, “Daen: Deep autoencoder networks for hyperspectral unmixing,” *IEEE Transactions on Geoscience and Remote Sensing*, vol. 57, no. 7, pp. 4309–4321, 2019. DOI: 10.1109/TGRS.2018.2890633.
- [19] Q. Jin, Y. Ma, X. Mei, and J. Ma, “Tanet: An unsupervised two-stream autoencoder network for hyperspectral unmixing,” *IEEE Transactions on Geoscience and Remote Sensing*, vol. 60, pp. 1–15, 2022. DOI: 10.1109/TGRS.2021.3094884.
- [20] K. Mantripragada and F. Qureshi, *Hyperspectral pixel unmixing with latent dirichlet variational autoencoder*, Mar. 2022.
- [21] X. Wang, Y. Zhong, L. Zhang, and Y. Xu, “Spatial group sparsity regularized nonnegative matrix factorization for hyperspectral unmixing,” *IEEE Transactions on Geoscience and Remote Sensing*, vol. 55, no. 11, pp. 6287–6304, 2017. DOI: 10.1109/TGRS.2017.2724944.
- [22] W. He, H. Zhang, and L. Zhang, “Total variation regularized reweighted sparse nonnegative matrix factorization for hyperspectral unmixing,” *IEEE Transactions on Geoscience and Remote Sensing*, vol. 55, no. 7, pp. 3909–3921, 2017. DOI: 10.1109/TGRS.2017.2683719.
- [23] X. Lu, H. Wu, Y. Yuan, P. Yan, and X. Li, “Manifold regularized sparse nmf for hyperspectral unmixing,” *IEEE Transactions on Geoscience and*

- Remote Sensing*, vol. 51, no. 5, pp. 2815–2826, 2013. DOI: 10.1109/TGRS.2012.2213825.
- [24] R. Borsoi, T. Imbiriba, and J. Bermudez, “Deep generative endmember modeling: An application to unsupervised spectral unmixing,” *IEEE Transactions on Computational Imaging*, vol. PP, pp. 1–1, Oct. 2019. DOI: 10.1109/TCI.2019.2948726.
- [25] D. M. Blei, A. Y. Ng, and M. I. Jordan, “Latent dirichlet allocation,” *J. Mach. Learn. Res.*, vol. 3, no. null, pp. 993–1022, Mar. 2003, ISSN: 1532-4435.
- [26] S. Woo, J. Park, J.-Y. Lee, and I. S. Kweon, *Cbam: Convolutional block attention module*, 2018. arXiv: 1807.06521 [cs.CV].
- [27] L. Pinheiro Cinelli, M. Araújo Marins, E. A. Barros da Silva, and S. Lima Netto, “Variational autoencoder,” in *Variational Methods for Machine Learning with Applications to Deep Networks*. Cham: Springer International Publishing, 2021, pp. 111–149, ISBN: 978-3-030-70679-1. DOI: 10.1007/978-3-030-70679-1_5. [Online]. Available: https://doi.org/10.1007/978-3-030-70679-1_5.
- [28] D. M. Blei, A. Kucukelbir, and J. D. McAuliffe, “Variational inference: A review for statisticians,” *Journal of the American Statistical Association*, vol. 112, no. 518, pp. 859–877, Apr. 2017. DOI: 10.1080/01621459.2017.1285773. [Online]. Available: <https://doi.org/10.1080/01621459.2017.1285773>.
- [29] C. Fox and S. Roberts, “A tutorial on variational bayes,” *Artificial Intelligence Review - AIR*, vol. 38, pp. 1–11, Aug. 2012. DOI: 10.1007/s10462-011-9236-8.
- [30] D. P. Kingma and M. Welling, *Auto-encoding variational bayes*, 2022. arXiv: 1312.6114 [stat.ML].
- [31] *Samson hsi dataset*. [Online]. Available: <https://rslab.ut.ac.ir/data>.
- [32] *Hydice urban hsi dataset*. [Online]. Available: <https://rslab.ut.ac.ir/data>.
- [33] *Cuprite dataset*. [Online]. Available: <https://rslab.ut.ac.ir/data>.
- [34] E. Bingham, J. P. Chen, M. Jankowiak, *et al.*, “Pyro: Deep Universal Probabilistic Programming,” *Journal of Machine Learning Research*, 2018.